ingegneria sismica
International Journal of Earthquake Engineering
Anno XLIII - Num. 2 - 2026

Molecular Design and Acid-Heat Synergistic Aging Mechanism of Silicone Adhesives with 500 °C Heat Resistance

Yaosheng Liang[1*], *Yongliang Sun*[1] *and Rong Sun*[1]

[1] Suzhou Thermal Power Research Institute Co., Ltd., Suzhou 215000, Jiangsu, China

SUMMARY: *For solving the problem that adhesive layers have early damage in hot-end sensor package, metal-ceramic connection, and heat-resisting insulation connection when they touch acid medium and discontinuous heat, this paper puts forward a kind of organosilicon adhesive system which has many phenyl groups, can be solidified through vinyl groups, and includes zirconium coordination nodes. The study investigates the mechanism underlying its 500 ℃ heat resistance and its acid-heat synergistic aging behavior. Using phenyltriethoxysilane, methyltriethoxysilane, and vinyltriethoxysilane as copolymerization monomers. Through controlled hydrolytic condensation, a phenylated siloxane prepolymer retaining a certain amount of Si-OH groups was prepared. Acetone-coordinated n-propanol zirconium was then introduced to construct Si-O-Zr nodes, yielding five formulations (P0-P4). Free-standing films and lap joints were prepared using a PMHS/Pt addition curing system. A synergistic aging protocol consisting of one cycle of "8 h acid immersion at 80 ℃+4 h heat treatment at 250 ℃" was established to characterize the chemical structure, thermal stability, post-heat bonding strength, interfacial evolution, and residual phase formation. The results indicate that P3 exhibits the best comprehensive performance under conditions of Ph/Si=0.40 and Zr/Si=0.06. This formulation had a double bond conversion rate of 93.8%, with 5% and 10% weight loss temperatures reaching 438 ℃ and 476 ℃, respectively; the residual carbon content at 800 ℃ was 56.8%, and the lap shear strength at room temperature was 8.54 MPa, which remained at 2.73 MPa after 30 minutes of thermal exposure at 500 ℃. After 15 cycles of synergistic aging, P3 retained 59.2% of its initial strength, with a synergy factor of 1.18, lower than the 1.34 for P0 and 1.29 for P1. The phenyl group increased the proportion of the high-temperature residual phase, while the Si-O-Zr nodes delayed the main weight loss zone and promoted the formation of a continuous Si/O/Zr-enriched layer on the surface; the acidic medium preferentially induces Si-O-Si hydrolysis and silanol enrichment at the surface and interface defects; the subsequent thermal phase further triggers re-condensation, oligomer escape, and volume shrinkage, ultimately manifesting as outer-layer hardening, increased modulus gradient, and expansion of the interfacial gap. This paper presents a formulation window and an acid-thermal coupled failure map applicable to thermal exposure conditions at 500 ℃.*

KEYWORDS: *organosilicon adhesive; 500 ℃ heat resistance; zirconium coordination; acid-thermal synergistic aging; failure mechanism*

1 Introduction

The assembling of hot-end electric heating parts, engine surrounding insulation sealings, exhaust-side sensor fixings, and ceramic insulation parts all need the adhesive layer to at the

*fengmi0921@126.com
https://doi.org/10.65102/is20261015
Published: 30 April, 2026

same time carry out the functions of wetting, load transferring, and keeping structural completeness after heat being exposed-all these inside a very thin shape. For these kinds of joint structures, the materials which are used confront complicated working environments. The starting and the stopping of equipment bring about temperature changes that are from 250 to 500 ℃. Acidic condensed liquid, acidic fog, or water vapor that carries acid can pass through the adhesive layer by edges and tiny pores, while the difference of thermal expansion between metal and ceramic or between metal and oxide materials continuously enlarges local stress. Traditional epoxy, phenolic, and acrylic type systems commonly display obvious volatilization and crack generation when temperature exceeds 300 ℃, hence this makes it hard to hold a continuous adhesive layer after the high-temperature situation occurs. Silicone materials, because they have the high bond energy of the Si-O main chain, a wide scope of composition regulation, and a certain trend toward inorganic change, therefore have a more practical basis for high-temperature adhesion [1, 2]. However, as for adhesive agents, simple "heat-resistant ability" is not enough. Whether the interfacial load-bearing ability can be kept after heat exposure often is dependent on the matching degree of three factors: network rearranging, residual layer generating, and interfacial condition.

Current studying of high-temperature silicone systems generally follows three main research directions. The first one includes controlling heat cracking paths via organic replacement groups, especially through raising the phenyl component to restrain high-temperature reverse-bonding depolymerization and increase the ratio of aromatic leftover layers. Relevant reviews and case studies indicate that the morphological retention capability of methylphenyl silicone resins and high-temperature liquid silicone rubbers in the 400-500 ℃ range is often closely related to phenyl content and crosslinking structure [3]. The second method includes bringing in different atoms with high bonding energy, for example Zr, to build more stable crosslinking nodes in the silicone network. The high-temperature stickiness glue that is built on zirconium-altered silicon resin which was reported by Jiang and other people proves that when Zr is got into the siloxane backbone, it greatly delays the starting time of the main weight loss area and promotes the reservation strength of the joint after the heat processing [4]; Gu and other authors. also discovered a same tendency in zirconium-altered silicon coverings, that is a more compact remaining layer and less surface breaking after high-temperature contact [5]. Third, the degree of ceramicization can be enhanced via polysilazanes or other precursor-like components, with the goal that the material may gradually turn into SiOC, SiCN, or zirconia-containing inorganic phases under higher temperature scopes [6-8]. These research achievements show that valid ways for promoting the working effect of high-temperature silicon-based materials are already completely built; however, when people use the same methods on adhesive matters, one must at the same time think over working viscous degree, surface wet situation, and solidify completeness, which greatly makes the range of workable solutions become much smaller.

This contraction of the design space originates principally from the service circumstances of thin adhesive layers. For covering layers or whole-body materials, so long as the entire-body heat stability is adequately high, partial decomposition does not certainly lead to instantaneous whole failure; however, regarding lap joints, the thicknesses of adhesive layers that lie between tens and more than one hundred micrometers cause that the interaction among surface reactions, volumetric shrinkage and interfacial delamination becomes more easy to occur. If the remainder layer of a high-temperature adhesive is not enough, it will quickly lose its cross-linking ability in the 400-500 ℃ environment; On the contrary side, if the leftover layer becomes thicker too quickly or the modulus gets larger far beyond normal, cracks can be spread out in the direction leading to the interface. At present, high-temperature precursor glue and ceramicizable organic glue systems have already obtained good outcomes in ceramic connection and heat protection

uses [9, 10], hence such systems usually need higher solid content, higher inorganic content, or thicker glue layers. For silicon ketone glue materials which must finish complete moistening and solidification inside a restricted film thickness, meanwhile keeping connecting part integrity at nearly 500 ℃, existent researches still provide limited specific resolutions about how to combine benzene radical enrichment, zirconium joint point introduction and crosslinking density control into one single formula window.

Beside the starting heat resistance, the chemical entering that happens during work can also change the later heat performance of the adhesive thin film. The studies about silicone rubber and silicone sealants have proven that acid water phases, hot humidity and temperature changes can accelerate the breaking of Si-O-Si bonds via hydrolysis, therefore generating more silanol groups, absorbed water, and moving paths for oligomer movement; After that, the heat contact lets the broken parts carry out more getting rid of silyl groups, re-condensation and part oxidation, therefore it brings slowly surface hardening and raised surface roughness and brittleness [11-16]. Although abundant experiment proof exists for these occurrences in sealing elements and heat insulation materials, to directly put them into use on high-temperature binding agents is still full of difficulties. This is on account of the fact that joint strength at the same time is controlled by the matrix network, the interface combining power, and the layer that remains after the heating process. If the acidic medium firstly opens the defect pathways that are near the surface and the interface, the thermal exposure that comes after will change the originally scattered chemical damage into the shrinkage cracks and the interfacial gaps that are more concentrated. At this juncture, the production of the remaining layer may either stop the whole structure from caving in or speed up the layer separation because the hardness of the outermost layer is too great. Current academic documents seldom discuss these two kinds of effects in the one same analyzing frame.

From this angle of view, the nowadays research has deficiency in no less than three aspects. First, as for silicone adhesives which are rated at 500 ℃, a continuous correlation that links molecular design with joint performance is something that does not exist. Up till the present moment, no usable formulation window has been established concerning in what way phenyl content, zirconium node content, residual Si-OH, and double bond conversion rate influence each other together. Second, although the combined actions of acid environments and heat circulation are often researched in sealing materials, quantitative contrasts of scaling rules for high-temperature adhesive connection parts are still absent. At last, the explanations of post-aging failure are often still stayed on the level of "strength decrease", there is not much deeper exploration about where cracks first produce, why the residual layer now brings good effect now brings bad effect, or when the interface completes the transformation from a secondary factor to a dominant factor. This present article deals with these problems.

This research chosen an organic silicon adhesive that is rich in phenyl groups, can be cured through vinyl groups, and has zirconium coordination nodes as the research object. Through the adjustment of Ph/Si and Zr/Si proportion values, five formulation groups (P0-P4) were constructed to carry out investigation on their load-bearing capability after heat processing at 500 ℃ and their acid-heat synergistic aging behavior. This research carries out study on three aspects: firstly, constructing a formula range which achieves balance among working feasibility, solidifying completeness and bearing capability after heating; second, what we do is compare degradation differences on the joint interface under three different routes-only acid, only heat, and acid combined with heat-and then use apparent damage rate constants and synergy factors to carry out quantification on them; third, through integrating chemical structure, thermal analysis, interfacial evolution and residual phase identification, we discuss the relationships among surface hydrolysis, thermal segment restructuring, shell growth and interfacial instability. The whole design idea and aging logic of this research are shown by Figure 1.

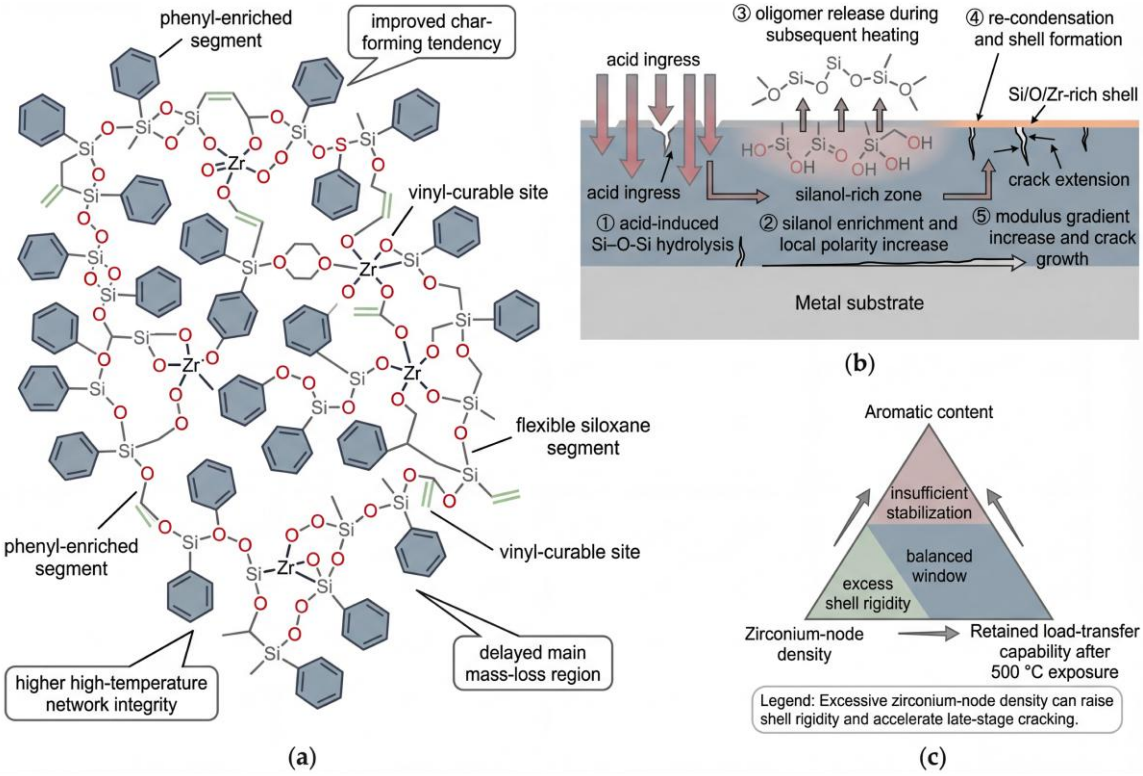

Figure 1: Molecular design and acid-thermal aging mechanism of the phenyl-rich zirconium-coordinated organosilicon adhesive.

2 Methods

2.1 Molecular design, resin synthesis, and formulation window

The data of this study is got from a standard experiment which includes five formulations (P0-P4). Among the five samples, the unique differences are the content of phenyl and the content of zirconium node; the density of vinyl, origin of the soft sections, kind of filling material, and solidification procedure were all maintained unchanged. This method was utilized by researchers to separate out the functions of "the thermal stability which is given by raised phenyl content," "the inorganic changing action of zirconium nodes," and "the bad influences which are brought by overmuch rigidity" inside the same formulation series. In the sample naming system, P0 and P1 are the control groups which do not have zirconium, while P2-P4 are the groups which are modified by zirconium.

The resin parent material was gotten through the co-hydrolytic polycondensation process of phenyl triethoxysilane, methyl triethoxysilane, and vinyl triethoxysilane. Because the high-temperature bonding layer must have the capability to produce aromatic residual phases and meanwhile keep enough cross-linking positions for addition reactions, therefore in this research the VTES feeding proportion was set as 0.16, and the Ph/Si ratio was regulated by changing the PTES/MTES ratio. We carried out the reaction in the xylene that had been dried, and the total solid content of the monomers was controlled at 45 wt%. The hydrolysis liquid is composed of deionized water and anhydrous ethyl alcohol, with the molar ratio of water to the sum of alkoxy groups being 1.0; the acting catalytic agent is 0.05 mol L-1 hydrochloric acid. The adding step is controlled to be 0-5 ℃ for reducing the danger of turbidity and gel formation which is brought by fast local condensation. After the adding work is finished, the system is kept at 25, 65, and 95 Celsius degree separately, to let the monomer slowly change from short-chain oligomers to

prepolymers that hold a certain degree of branch structure and leftover Si-OH groups. The complete condensation work is not what this stage pursues; the purpose is to keep the active positions that are needed for later reaction combination with the zirconium precursor.

For the sake of lifting the proportion of zirconium that is got into the siloxane network, the zirconium source which is used is n-propanol zirconium that is stabilized with acetone. First, n-propanol zirconium has been subjected to pre-complexation with acetylacetone under a mole proportion of 1:1.2 for duration of 30 minutes in a temperature of 50 ℃. The solution which we have obtained is then added by drops to the above-mentioned prepolymer that contains silanol, and the reaction is kept going for 2 hours at 75 ℃ in the atmosphere of nitrogen. This handling was put forward on the basis of two points of consideration: first, it is to lower the speed of self-condensation of zirconium alcoholate and hence prevent the partial gathering of zirconium oxide; Second, in order to make the Zr-OR reaction go more in the direction of Si-OH condensation, thus it can form Si-O-Zr nodes. When the reaction finished, the remained acid was neutralized by triethylamine, and components with low boiling point were got rid of through decompressing, make the viscosity of resin at 25 ℃ to be controlled in the scope of 5-11 Pa·s. If the viscosity goes beyond this scope, uneven painting thickness will happen when scraping; if its value drops under this interval, even though the surface flatness effect is satisfying, it will bring decrease to the stability of edge thickness and the continuous property of the residual layer after curing [17-19].

To facilitate comparison of the structural states of different formulations, the following parameters are defined: phenyl substitution degree ϕ_{Ph}, zirconium coordination ratio χ_{Zr}, and double bond conversion rate α_{Vi}:

$$\phi_{Ph}=\frac{n_{Ph}}{n_{Si}} \tag{1a}$$

$$\chi_{Zr}=\frac{n_{Zr}}{n_{Si}} \tag{1b}$$

$$\alpha_{Vi}=1-\frac{(A_{1603}/A_{1258})_t}{(A_{1603}/A_{1258})_0} \tag{1c}$$

In the equation, n_{Ph} represents the number of moles of phenyl structural units, n_{Si} represents the total number of moles of silicon atoms in the system, and n_{Zr} represents the number of moles of zirconium atoms involved in network formation; A_{1603} and A_{1258} represent the peak areas of the vinyl and Si-CH_3 characteristic peaks in the FTIR spectrum, respectively, with the subscripts 0 and t denoting before and after curing, respectively. The synthesis and curing route of the PhZr-VSi adhesive is shown in Figure 1.

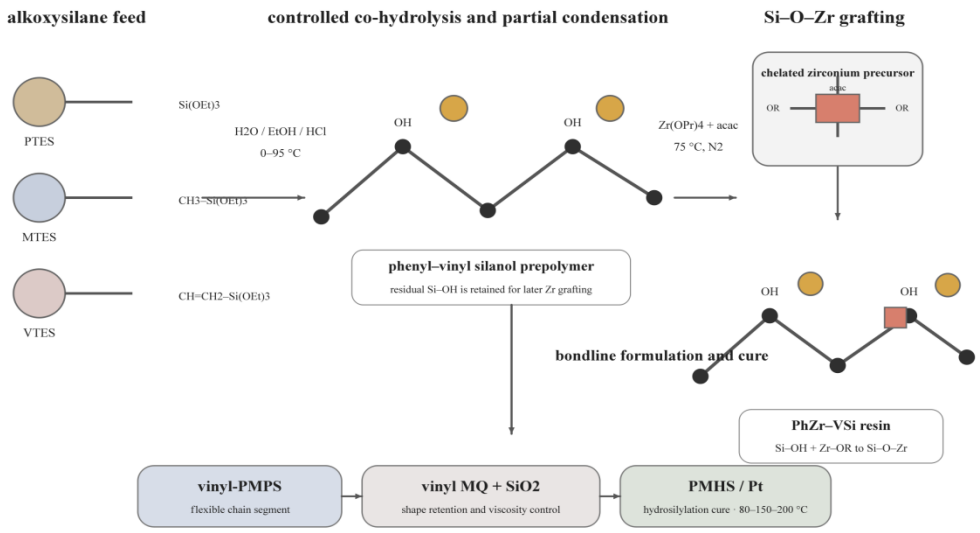

Figure 2: Synthesis and curing route of the PhZr-VSi adhesive.

In formulating the adhesive, a self-prepared PhZr-VSi resin was used as the matrix phase, 18 wt% vinyl-terminated polymethylphenylsiloxane was incorporated as a flexible segment, 12 wt% vinyl MQ resin was added to enhance initial lap strength and post-curing film continuity, and 10 wt% hydrophobic vapour-deposited SiO_2 was included to regulate rheology and prevent edge collapse. The cross-linking agent was polymethylhydrosiloxane, with an H/Vi ratio set at 1.15; the catalyst was a Pt complex, at 25 ppm Pt; and the inhibitor was added at 0.08 pbw. After mixing, the compound was degassed for 20 minutes at -0.095 MPa. The reason for fixing the H/Vi ratio rather than varying all parameters simultaneously was to avoid confounding 'under-curing due to insufficient cross-linking agent' with 'structural differences caused by aromatisation or zirconium nodes'.

The design of P0-P4 does not aim to maximise any single parameter. P0 and P1 are used to establish the upper limit and reference for the basic methyl/phenyl siloxane network; P2 and P3 are used to investigate whether the system can improve its thermal retention at 500 ℃ without significantly compromising workability following the introduction of small and moderate amounts of Zr nodes; P4 is used to observe whether premature embrittlement occurs under conditions of high phenyl and high Zr content. Table 1 lists the formulation parameters for the five groups of samples. As shown in Table 1, with increasing Ph/Si and Zr/Si ratios, the residual Si-OH content gradually decreased from 1.52 mmol g^{-1} to 0.88 mmol g^{-1}, the viscosity increased from 5.8 Pa·s to 10.2 Pa·s, and the gelation time at 120 ℃ shortened from 28 min to 21 min. P3 lies in the middle of this range of variation and is therefore considered a candidate point that may balance workability and high-temperature retention.

Table 1: Formulation matrix and key compositional parameters of the PhZr-VSi adhesives

Sample	PTES/MTES/VTES (mol/mol/mol)	Ph/Si	Zr/Si	Residual Si-OH (mmol g−1)	Viscosity at 25 ℃ (Pa·s)	Gel time at 120 ℃ (min)	C=C conversion (%)
P0	0.20/0.64/0.16	0.20	0.00	1.52	5.8	28	89.1
P1	0.30/0.54/0.16	0.30	0.00	1.37	6.4	25	91.8
P2	0.35/0.49/0.16	0.35	0.03	1.08	7.1	23	93.1
P3	0.40/0.44/0.16	0.40	0.06	0.92	8.0	22	93.8
P4	0.45/0.39/0.16	0.45	0.08	0.88	10.2	21	91.2

2.2 Curing, joint preparation, and acid-thermal aging protocol

In order to guarantee the comparability of mechanical testing outcomes among different formulations, a unified sample preparation flow was utilized for both the free membrane and the connecting parts. The free thin layer was rotated and covered in a polytetrafluoroethylene container, with the moist layer thickness being controlled at 0.45 mm; After the completion of curing process, the thickness value was 0.40±0.03 mm. This membranous sample was utilized for the analyses of FTIR, XPS, TGA, DMA and XRD. The lap connection pieces were manufactured by use of 304 stainless steel single-lap test pieces, which measure 100×25×1.5 mm, and have an overlapping area of 12.5×25 mm. Before the bonding operation, the test test-pieces were in order polished by 1000-grit sandpaper, then blasted by 120-mesh grit sand, put into ultrasonic processing in acetone for 15 minutes, and finally dried under 60 ℃ for 30 minutes, thus the surface roughness is controlled at Ra=1.8±0.2 μm. When people carry out the adhesive daubing work, glass microspheres that have an average granule dimension of 120 μm were put in to carry out the control of the thickness of adhesive layer, therefore this brings about a final thickness of adhesive layer that is 120±10 μm.

The curing system that lets material harden was composed of a three-step temperature ascending: 80 ℃ held for 1 hour, 150 ℃ held for 2 hours, and 200 ℃ held for 2 hours. The first stage was purposely planned to stop the system from forming gel too quickly in the low-viscosity stage and gathering too much inner stress; the second stage, it was designed for finishing the main addition curing reaction; and the third stage has the function of getting rid of low-molecular-weight remaining substances and strengthening the completeness of the network. All joint specimens were permitted to rest for 24 hours following the completion of curing before they were subjected to lap shear testing which was carried out at room temperature. Heat exposure experiments were carried out in an air environment at temperature spots of 300, 400 and 500 ℃, with a preserve time of 30 minutes at each spot, then naturally cool down to indoor temperature and carry out measurement of lap joint strength. In the condition of each temperature point, no less than seven independent joints were carried out experiments, and the results that we got are expressed as average values.

Acid-heat synergistic ageing is designed to simulate operating conditions where pre-damage caused by acidic media coexists with subsequent thermal restructuring. The ageing medium consists of an aqueous mixture of H_2SO_4 and HNO_3, with a pH of 2.5 at room temperature; a single cycle comprises four steps: 8-hour acid immersion at 80 ℃, 30-second rapid rinsing with deionised water, 1-hour drying at 60 ℃, and 4-hour heat treatment in an air atmosphere at 250 ℃. Compared to simply leaving samples in a constant-temperature acid solution for an extended period, this protocol more closely approximates the conditions experienced by actual equipment, which alternates between chemical attack and intermittent heating. To distinguish between single-factor and coupled effects, two control groups-‘acid-only’ and ‘heat-only’-were established; the three groups of samples were consistent in terms of sampling points and characterisation parameters. Samples of the free membrane and the joint were taken after the 1st, 5th, 10th and 15th cycles for mass, contact angle, DMA, XPS, SEM/EDS and mechanical testing.

High-temperature retention and ageing degradation are primarily evaluated by comparing the strength retention rate following thermal exposure at 500 ℃ with that under cyclic ageing, expressed as follows:

$$\eta_{500}=\frac{\tau_{500}}{\tau_{RT}}\times 100\% \tag{2a}$$

$$R_{\tau}(n)=\frac{\tau_{n}}{\tau_{0}}\times 100\% \tag{2b}$$

In this context, τ_{500} and τ_{RT} denote the lap shear strength after thermal exposure at 500 ℃ and at room temperature, respectively, whilst τ_n and τ_0 denote the lap shear strength before ageing and after the nth cycle, respectively. The rate of mass change and the retention of energy storage modulus are calculated from the relative changes in dry mass and the energy storage modulus at 25 ℃ before and after ageing, respectively. To compare the rates of degradation under different ageing pathways, this paper performs exponential fitting on the variation of strength retention with the number of cycles, and characterises the ageing rate using the apparent damage rate constant.

The fracture mode is determined by the area fraction of the fracture surface. Aggregation failure is defined as a residual colloid area greater than 70%, while interfacial failure is defined as a residual colloid area less than 30%; all other cases are classified as mixed failure. To minimise errors caused by edge defects in individual fracture images, at least five joint fracture surfaces are analysed per group.

2.3 Multi-scale characterization and data reduction

The characterisation work of this our study concentrated on three key problems: if a cross-linked network has already formed; How much portion of the network was still kept after the high-temperature treatment; and how the damage on interface was developed after the cycles of acid and heat. ATR-FTIR was utilized by researchers for tracing characteristic absorption peaks of benzene rings, vinyl transformation, and peaks related to Si-O-Zr bond, whose measurement scope is 4000-500 cm^{-1} and whose resolution is 4 cm^{-1}; For each sample, the scanning operation was carried out 32 times by us. X-ray photoelectron spectroscopy was utilized to carry out analysis of the surface chemical condition after Zr was introduced and the alterations of O/Si and C/Si atom proportions before ageing and after ageing. The experiment employed an AlKα radiation source, and the correction of binding energy was carried out by making use of C 1s under 284.8 eV. For the guarantee of comparability among different samples, all XPS peak fittings have used identical Shirley background and peak width restriction conditions; The Zr 3d peak has been carried out separation into $3d_{5/2}$ and $3d_{3/2}$ doublets, for the purpose of determining the bonding state of Zr in the inside of the silicate.

Thermal analysis was performed using a combination of TGA, DTG and TG-FTIR. TGA was conducted in a nitrogen atmosphere, heating at a rate of 10 ℃ min^{-1} to 800 ℃, recording the temperatures at 5% and 10% mass loss, and the residual mass fraction at 800 ℃. DTG peak positions were used to determine whether the main pyrolysis zone had shifted to higher temperatures, whilst TG-FTIR focused on monitoring the signals of volatile cyclic siloxanes in the 350-600 ℃ range to assess the extent of back-biting depolymerisation [24, 25]. To compare the ability of different formulations to form an inorganic residue layer, this study used the residual carbon content to characterise the residue level at 800 ℃:

$$f_c = \frac{m_{800}}{m_0} \times 100\% \tag{3}$$

In the equation, m_{800} represents the residual mass at 800 ℃, and m_0 represents the initial mass. The DMA was conducted in tensile mode, with a test frequency of 1 Hz and a temperature range of 25-350 ℃. In addition to comparing changes in the energy storage modulus at 25 ℃ and 300 ℃, this study further estimated the apparent cross-linking density using the energy storage modulus at 200 ℃ to reflect the level of effective network structure still capable of participating in load transfer within the medium-to-high temperature range:

$$\nu_e = \frac{E'_r}{3RT_r} \tag{4}$$

In the equation, E'_r represents the energy storage modulus at the reference temperature T_r, and R is the gas constant. In this paper, T_r is taken as 473.15 K. Compared with a simple comparison of the residual carbon content, this parameter is more useful for distinguishing between formulations with 'higher residual mass but a significantly looser support network' and those with 'slightly lower residual mass but better post-heating network continuity'.

The interface and fracture surface morphology were characterised using SEM/EDS. Fracture specimens were gold-sputtered following brittle fracture in liquid nitrogen, whilst cross-sectional specimens were embedded in resin and polished. The crack area fraction, average interfacial gap width and growth rate of the surface residual layer thickness were used to characterise the extent of surface cracking, the degree of interfacial debonding and the thickening trend of the inorganic enrichment layer during ageing, respectively. The crack area and gap width were calculated based on statistics from 10 randomly selected fields of view, whilst the residual layer thickness was determined by averaging 20 measurement points. To compare the extent of amplification between single-factor ageing and coupled ageing, this study introduces a synergy factor:

$$S_k = \frac{k_{a+h}}{k_a + k_h} \tag{5}$$

In the equation, k_{a+h}, k_a and k_h represent the apparent damage rate constants obtained from strength decay fitting under acid-thermal, acid-only and heat-only conditions, respectively. A value of S_k>1 indicates a synergistic effect between acid and heat that exceeds simple superposition. Based on this, failure maps are constructed in the following sections by combining the residual carbon content and the strength retention level after ageing, which are used to determine the service limits for different formulations.

All mechanical results were obtained from seven independent joints, with spectroscopic and morphological parameters repeated at least three times. Data are presented as mean ± standard deviation; intergroup differences were compared using one-way analysis of variance (ANOVA), with P<0.05 considered statistically significant.

3 Results and Discussion

3.1 Network construction and realization of 500 ℃ heat resistance

Before delving into the ageing mechanism, two issues must first be confirmed: whether the phenyl units and Zr nodes have indeed incorporated into the network; and whether this structural change is sufficient to translate into joint retention capacity that remains detectable even after heating to 500 ℃. Figure 3 provides direct evidence of this.

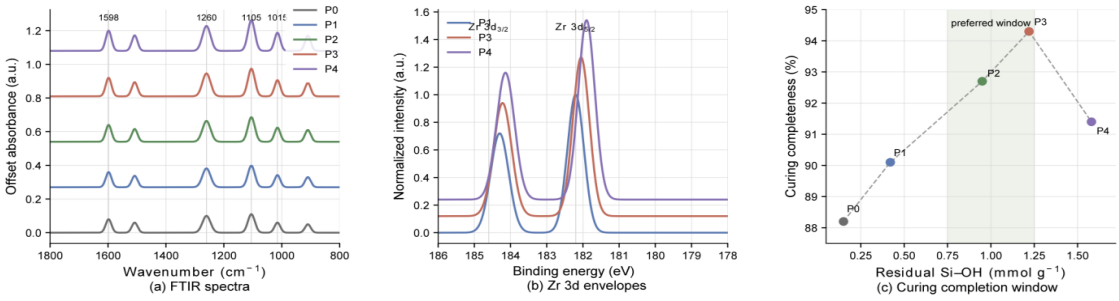

Figure 3: Structural signatures of phenyl/Zr incorporation and curing completion in the PhZr-VSi adhesives.

In Figure 3(a), the characteristic peaks of benzene ring at 1595 and 1430 cm^{-1} from P0 to P4 gradually have increased intensity, hence it shows that the bringing in of aromatic units is a continuous process; At the same time, P2-P4 display a clear hump at 952 cm^{-1}, but P0 and P1 almost have no this characteristic, hence it shows that adding Zr has produced an identifiable Si-O-Zr bond. In the Figure 3(b), the Zr 3d area of P1 only presents a flat base line, but P3 and P4 show pairing peaks at 184.3 eV and 182.2 eV, which accords with the Zr $3d_{3/2}$/$3d_{5/2}$ division feature. This shows that Zr exists in the surface network by means of chemical bonds, hence it is not only just as leftover free inorganic phases. Figure 3(c) further compares the residual Si-OH content with the double-bond conversion rates on the same plot. The C=C conversion rates for P0, P1, P2, P3 and P4 were 89.1%, 91.8%, 93.1%, 93.8% and 91.2% respectively, corresponding to residual Si-OH levels of 1.52, 1.37, 1.08, 0.92 and 0.88 mmol g^{-1}. The conversion rate peaked at P3 and subsequently declined at P4, indicating that when both the phenyl and Zr nodes were raised to higher levels, local chain segment mobility was restricted, and late-stage cross-linking was consequently impeded. This structural difference was subsequently reflected in thermal stability and the retention of high-temperature modulus, as shown in Figure 4.

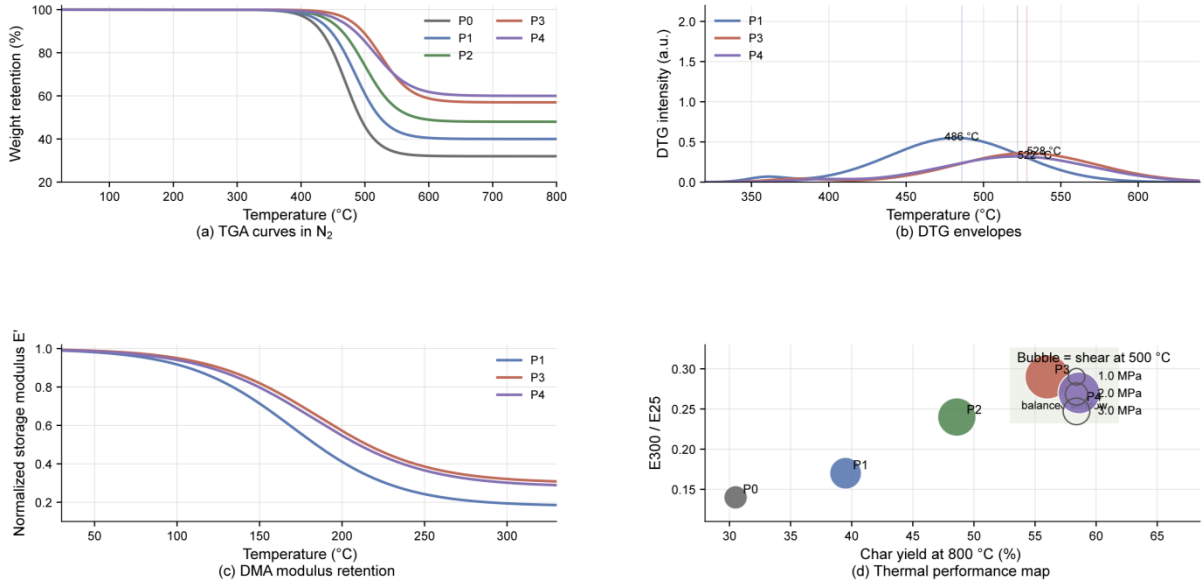

Figure 4: Thermal stability, DTG delay, and thermomechanical retention of the PhZr-VSi adhesives.

In Figure 4(a), the TGA curve for P0 begins to decline rapidly at around 450 ℃, retaining only approximately 31% of its mass after 600 ℃; as the number of phenyl and Zr units increases, the weight loss curve shifts laterally as a whole, with P3 and P4 retaining approximately 57% and 59% of their mass, respectively, at around 600 ℃. The DTG envelope in Figure 4(b) further illustrates the changes in the main decomposition region: the main peak for P1 is at 486 ℃, whilst that for P3 shifts to 528 ℃ and for P4 to 534 ℃. This indicates that the Zr nodes do indeed retard the main weight loss process, but the improvement observed in P4 compared to P3 is significantly reduced. In Figure 4(c), the normalised storage modulus of P1, P3 and P4 continues to decrease with rising temperature; at 300 ℃, the corresponding E'300/E'25 ratios are 0.17, 0.29 and 0.27, respectively. In other words, whilst the residual carbon content of P4 continues to increase, the thermal-mechanical retention does not improve in tandem. Figure 4(d) plots the residual carbon content, high-temperature modulus retention and 500 ℃ lap strength on the same graph. It can be seen that P3 lies within the equilibrium zone where ‘the residual

layer is sufficient and modulus retention remains acceptable', whilst P4 is approaching the boundary where high residual carbon content is accompanied by a decline in high-temperature load-bearing capacity. The summary results of the thermal analysis and mechanical testing are shown in Table 2.

Table 2: Thermal and adhesive properties of different formulations

Sample	T_5%(℃)	T_{10}%(℃)	Char yield at 800 ℃ (%)	E300′/E25′	ν_e at 200 ℃ ($\times 10^4$ mol m^{-3})	τRT (MPa)	τ500 (MPa)
P0	374	417	31.4	0.14	1.73	5.61	0.86
P1	398	443	39.7	0.17	2.07	6.47	1.42
P2	421	461	48.6	0.24	2.52	7.36	2.11
P3	438	476	56.8	0.29	2.84	8.54	2.73
P4	444	481	59.3	0.27	2.73	7.92	2.41

In Table 2, the T5% and T10% values for P3 reached 438 and 476 ℃ respectively, with a residual carbon content of 56.8% at 800 ℃; this formulation strikes a balance between the initial weight loss temperature and the proportion of material retained at high temperatures. Its apparent cross-linking density at 200 ℃ reached 2.84×10^4 mol m^{-3}, which is higher than that of P1 2.07×10^4 mol m^{-3}. This result indicates that the advantage of P3 lies not only in the formation of a greater residual layer during the high-temperature stage, but more importantly in the fact that it retains a more continuous supporting network in the medium-to-high temperature range. Figure 5 provides a more direct illustration of the cross-linking performance.

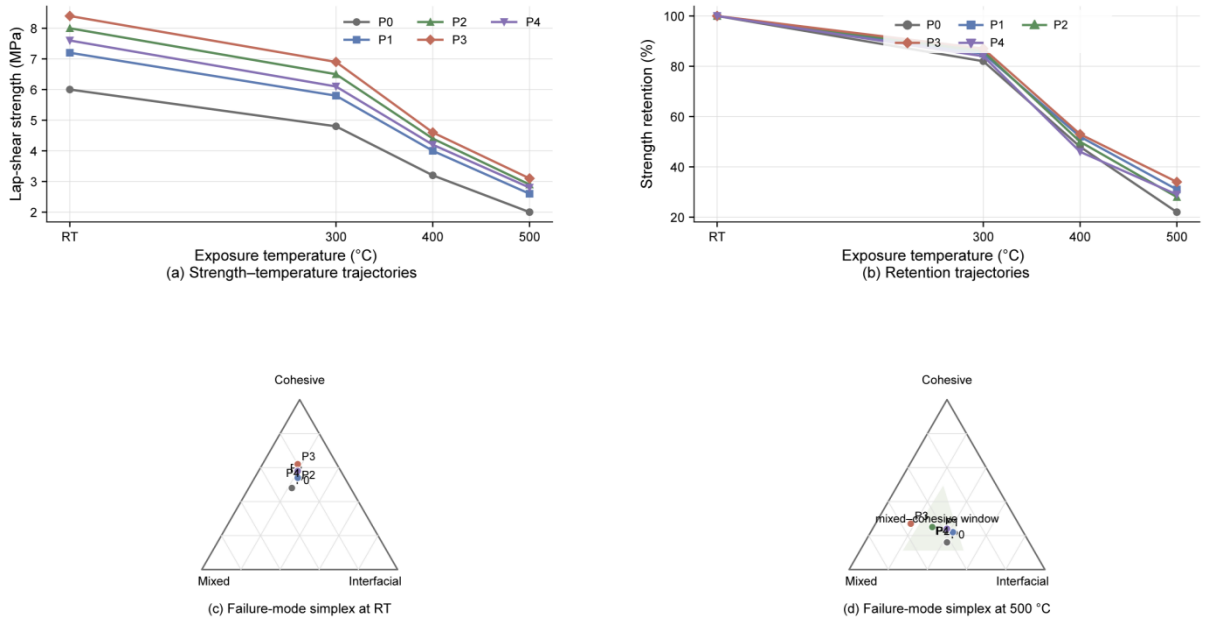

Figure 5: Temperature-dependent lap-shear trajectories and failure-mode simplex maps of the bonded joints.

In Figure 5(a), the room-temperature lap shear strength of P3 was 8.54 MPa; after 30 minutes of thermal exposure at 300, 400 and 500 ℃, it remained at 6.92, 4.38 and 2.73 MPa respectively; The corresponding values for P1 were 6.47, 5.03, 3.01 and 1.42 MPa, whilst P0 decreased from 5.61 MPa to 0.86 MPa. When converted to retention rates, Figure 5(b) shows

that P3 retains 32.0% of its room-temperature strength at 500 ℃, P2 retains 28.7%, P1 retains 21.9%, and P0 retains 15.3%. This disparity is consistent with the trend in residual carbon content but is not simply equivalent to it. P4 had the highest residual carbon content at 800 ℃, yet retained only 30.4% of its room-temperature strength, slightly less than P3. The fracture modes shown in Figures 5(c) and 5(d) further explain this difference. At room temperature, the fracture mode of P3 was 81% agglomeration, 14% mixing and 5% interface, with the interior of the gel layer remaining the primary failure site; after thermal exposure at 500 ℃, P3 changed to 24% agglomeration, 54% mixing and 22% interface, indicating that the influence of the interface had increased, but the gel layer still retained a certain amount of bridged residual layer. In contrast, after 500 ℃, P0 exhibited 5% agglomeration, 25% mixed and 70% interfacial failure, whilst P1 showed 8% agglomeration, 32% mixed and 60% interfacial failure, with the interface becoming the dominant failure location. The situation for P4 lies between that of P2 and P3; the proportion of interfacial failure after 500 ℃ reaches 38%, indicating that excessive stiffness leads to earlier hardening of the outer layer, making it easier for cracks to propagate along the interface. The effective window for 500 ℃ heat-resistant silicone adhesives does not lie in ‘the higher the degree of aromatisation, the better’, nor in ‘the more inorganic nodes, the better’. The reason P3 performed best is that this formulation strikes a more reasonable balance between curing completeness, delayed thermal weight loss, residual layer continuity and high-temperature modulus retention.

3.2 Adhesion decay and interface evolution under acid-thermal coupling

Having completed the post-heat screening, the next step is to determine how the acidic medium and thermal cycling jointly alter the state of the joint. There are three key points of interest here: the extent to which strength degradation exceeds that caused by single-factor ageing; whether the degradation manifests primarily as bulk changes or interfacial changes; and whether different formulations exhibit the same sensitivity to this coupled amplification. Figure 6 first illustrates the trajectory of changes in macroscopic properties.

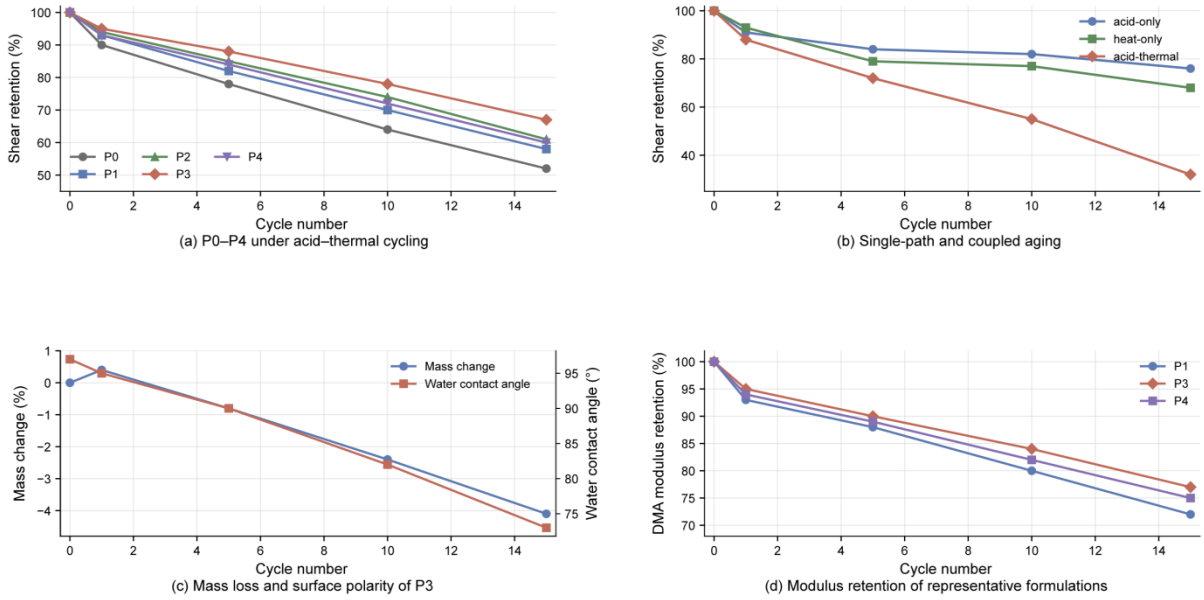

Figure 6: Strength decay, mass evolution, surface polarity, and modulus retention under acid-thermal cycling.

In Figure 6(a), under acid-heat coupling conditions, the strength retention rates of P0-P4 all

along decrease as the number of cycles increases, but the degrees of decline have very big differences. When the fifth circulation had been completed, the hold percentages for P0, P1, P2, P3 and P4 were 71.6%, 77.3%, 82.8%, 86.2% and 83.9% each one separately; When the 10th cycle was arrived at, these numerical values had become 52.4%, 59.5%, 66.4%, 72.8% and 68.1%; by the 15th cycle, they had a further decrease to 35.6%, 43.8%, 53.7%, 59.2% and 55.1%. P3 was shown to have the most slow decrease in the whole ageing course, hence this shows that it kept a bigger structure storage between the step of acid pre-damage and the step of heat restructuring. The calculated apparent damage rate constants obtained under synergistic ageing conditions similarly displayed a gradual decreasing trend from P0 to P3, which was followed by a small rebound at P4: the value of P0 was 0.0688 $cycle^{-1}$, the value of P1 was 0.0549 $cycle^{-1}$, P2 was at 0.0414 $cycle^{-1}$, P3 was at 0.0350 $cycle^{-1}$, and P4 has risen to 0.0398 $cycle^{-1}$. The increment which was found in P4 indicates that when the shell rigidness is too high, the crack spreading speed is again increased in the later phases of ageing.

Figure 6(b) plots the three curves for P3-acid-only, heat-only and acid-thermal-on the same coordinate system. At the 5th cycle, the retention rates for the three were 92.4%, 89.1% and 86.2% respectively, with the gap remaining small; by the 10th cycle, this gap had widened to 88.9%, 85.2% and 72.8%; by the 15th cycle, they had ultimately reached 83.5%, 77.4% and 59.2%. The same material did not exhibit such a steep decline under either acid-only or heat-only conditions, indicating that the acidic medium alone does not cause significant strength loss; rather, the subsequent thermal stage is dealing with a damaged region that is more prone to shrinkage and cracking. The synergy factors in Table 3 further quantify this: *Sk* for P3 is 1.18, for P2 is 1.24, for P1 is 1.29, and for P0 is 1.34. The looser the underlying network and the thinner the residual layer, the stronger the amplification effect between acid and heat.

Figures 6(c) and 6(d) illustrate the changes in bulk phase state during the degradation process. The mass of P3 increased slightly after the first cycle, by 0.34%, which is related to the penetration of the acid solution into the surface layer and the subsequent increase in water-holding capacity due to the rise in polar sites. As the cycles progressed, oligomer precipitation and surface peeling gradually became dominant, with the mass decreasing to -0.62%, -1.47% and -2.31% after the 5th, 10 and 15 cycles, the mass changes to -0.62%, -1.47% and -2.31% respectively. During the same process, the water contact angle decreases from 98.4° to 92.1°, 85.6°, 75.8° and 68.4°, indicating that the surface layer is continuously transitioning to a state of higher polarity. The DMA retention rates shown in Figure 6(d) indicate that the modulus retention rates of P1, P3 and P4 after 15 cycles were 49.3%, 64.7% and 60.5% respectively. The fact that P3 is higher than P1 indicates that its load-bearing network degrades more slowly; the fact that P3 is higher than P4 indicates that moderate shell hardening helps to maintain modulus, whereas excessive stiffness triggers local cracking at an earlier stage. The interface evolution corresponding to macroscopic degradation is shown in Figure 7.

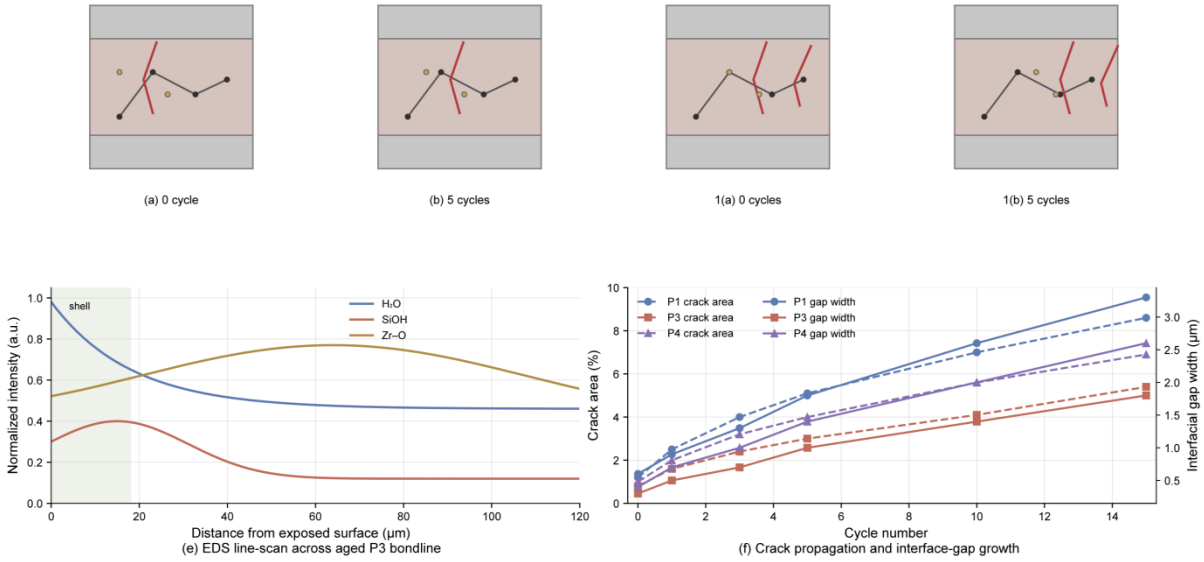

Figure 7: Bondline evolution, EDS line-scan, and crack-growth metrics during coupled aging.

Figures 7(a) to 7(d) illustrate the evolution of the cross-section of the rubber layer after 0, 5, 10 and 15 cycles, using P3 as an example. In the unaged sample, the upper and lower interfaces of the rubber layer are continuous, and the network extends across the entire thickness; after 5 cycles, a thin oxygen-rich layer begins to form on the surface-which is preferentially affected by the acid solution-with localised shrinkage cracks appearing, whilst the interface remains largely continuous; after 10 cycles, the oxygen-rich layer coalesces into patches near the surface, and volumetric shrinkage in the thermal zone leads to an increase in the number of cracks; after 15 cycles, a more continuous residual shell forms on the surface, with more pronounced open gaps visible near the interface. The EDS line scan in Figure 7(e) is consistent with this observation. Taking the aged P3 sample as an example, a marked enrichment of the O signal is observed within the range of 0-16 μm from the exposed surface; simultaneously, Zr retains a discernible shoulder in the near-surface layer, whilst Si maintains a relatively flat plateau between 40 and 70 μm. This indicates that a Si/O/Zr transition zone has formed in the surface layer of P3, rather than a sharp, brittle boundary. In contrast, the transition zone in P1 is narrower, whilst the surface enrichment in P4 occurs more rapidly but with a steeper gradient.

Figure 7(f) plots the crack area fraction and the interfacial gap width against the number of cycles on the same graph. The crack area of P3 was 3.2%, 5.7% and 8.7% after the 5th, 10 and 15 cycles, with corresponding average interface gaps of 1.1, 1.6 and 2.1 μm; for P1, the crack area was 6.8%, 12.9% and 17.9%, with interface gaps reaching 2.6, 4.3 and 5.8 μm; P4's crack areas were 4.3%, 8.1% and 12.3%, with interface gaps of 1.4, 2.2 and 2.9 μm. Although P4's interface gap was significantly smaller than that of P1, its crack area remained higher than that of P3, indicating that when the shell layer is excessively hard, cracks are more likely to remain confined to the surface layer and the shell/core transition zone, rather than fully propagating into a wide interface gap. The primary issue with P1, however, is insufficient residual layer; once a crack forms, it is more likely to directly induce delamination at the interface.

As can be seen from Figures 6 and 7, acid-thermal coupled damage is not controlled by a single factor; the two processes take turns dominating at different stages of the cycles. In the first few cycles, increased polarity, a slight increase in mass and a decline in modulus are the more significant characteristics; in the middle and later stages, the escape of oligomers, thickening of the shell layer and widening of the interfacial gap gradually become the primary issues. The advantage of P3 lies in the ability of the surface layer to form a continuous but not

excessively rigid residual layer, thereby suppressing crack propagation velocity and prolonging the retention time at the interface.

3.3 Chemical degradation, residual-phase evolution, and failure map

The previous section presented the performance decay curves and the evolution of the interface position; this section continues to investigate the chemical origins of these changes, as shown in Figure 8.

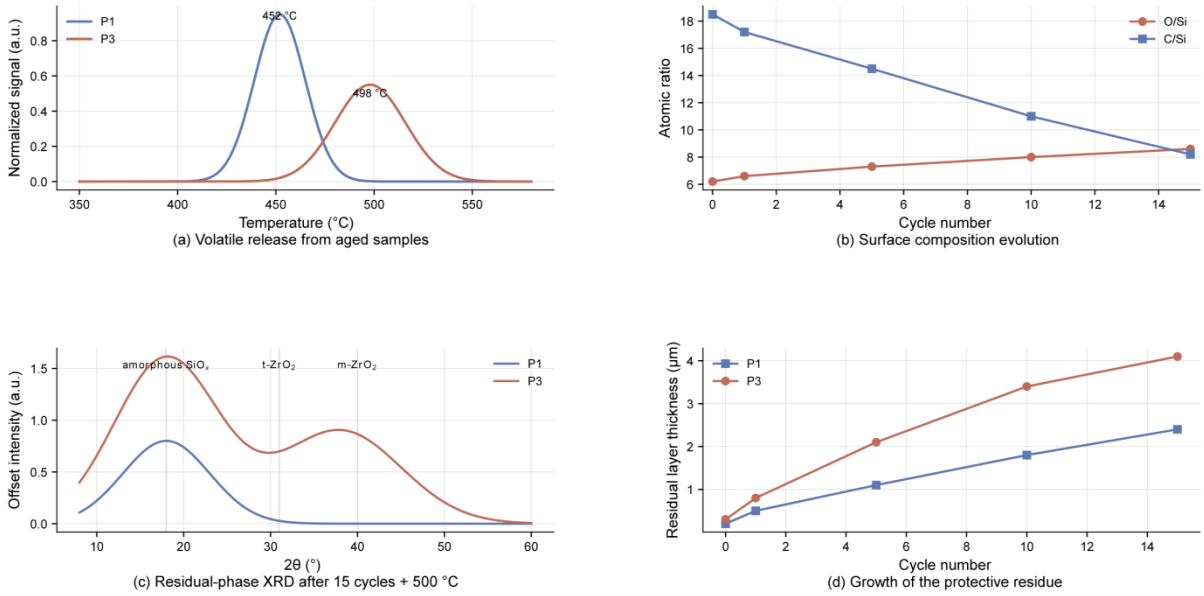

Figure 8: Volatile release, surface composition shift, residual-phase formation, and protective-shell growth during coupled aging.

Figure 8(a) first compares the release behaviour of volatile cyclic siloxanes from aged samples in the 350-600 ℃ range. The main release peak for P1 is located at 452 ℃, whereas for P3 it shifts to 498 ℃ and exhibits a broader peak shape. The shift in peak position indicates that the onset of main-chain cleavage and the escape of small molecules in P3 is delayed; the broadening of the peak shape suggests that the volatilisation process is no longer concentrated within a narrow temperature range, which is consistent with the fact that networks containing Zr nodes are less prone to rapid back-biting depolymerisation. Figure 8(b) further illustrates the cyclic evolution of the surface composition of P3. The O/Si ratio gradually increased from 1.38 (prior to ageing) to 1.45, 1.52, 1.64 and 1.73, whilst the C/Si ratio decreased sequentially from 1.92 to 1.81, 1.62, 1.40 and 1.21. This change indicates that, on the one hand, the surface layer continues to oxidise and accumulate Si-O structures, whilst on the other hand, organic side chains and oligomeric volatiles continue to decrease. It is precisely because this process occurs gradually that P3 can form a relatively continuous inorganic enrichment layer on the surface, avoiding a direct transition to a loose, powdery layer.

Figures 8(c) and 8(d) correlate this surface evolution with the morphology of the residual phase. After undergoing 15 ageing cycles followed by treatment at 500 ℃, the XRD pattern of P3 exhibits not only a stronger amorphous SiO_x scattering band near 22°, but also discernible t-ZrO_2 characteristic peaks near 30.2° and 50.3°. The residual phase in P1 is primarily manifested as a weaker SiO_x scattering band, with no obvious zirconia-containing crystalline phase features. In terms of shell thickness, the residual layer thicknesses of P1 after the 1st, 5th, 10th and 15th cycles were 0.4, 1.4, 2.2 and 2.8 μm, respectively, whilst those of P3 were 0.7,

2.3, 4.7 and 6.3 μm. P3 is more prone to forming a continuous shell layer and therefore retains higher cross-linking capacity after both thermal exposure at 500 ℃ and synergistic ageing. At the same time, an increase in shell thickness does not necessarily lead to better results. The surface layer of P4 enriched more rapidly, but the crack area remained higher than that of P3 after 15 cycles, indicating that as shell rigidity increases, the shell/inner layer transition zone becomes a new weak point. To place formulation differences, residual layer capacity and ageing sensitivity within a single framework, Figure 9 establishes two complementary coordinates

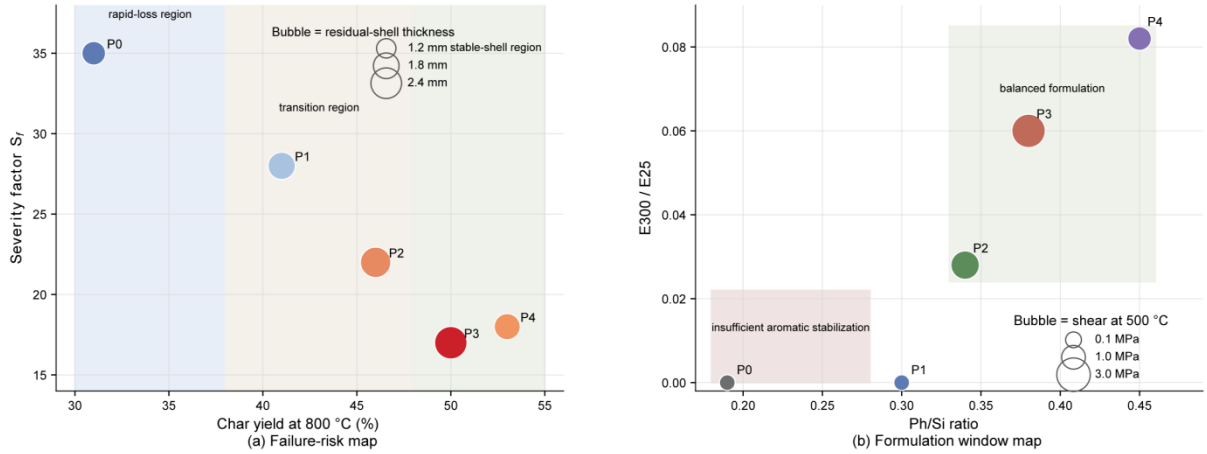

Figure 9: Synergy-controlled failure map and formulation window for 500 ℃ service.

Figure 9(a) plots the residual carbon content at 800 ℃ on the x-axis, the synergistic factor Sk on the y-axis, and the retained strength after 15 cycles as bubble size, with the plot shaded according to the crack area fraction. P0 is located in the ‘low residual phase, high synergy amplification’ region, with a residual carbon content of only 31.4%, a synergy factor of 1.34, and a retained strength of only approximately 2.00 MPa after 15 cycles. For P1, the residual carbon content increases to 39.7%, but as the residual layer remains insufficient, the retained strength is also only 2.83 MPa. P2 enters the transition zone, indicating that a small amount of Zr nodes is already capable of reducing coupling amplification. P3 is located in the equilibrium zone, with a residual carbon rate of 56.8% and a synergy factor of 1.18; after 15 cycles, the retained strength is approximately 5.06 MPa, and the crack area is the lowest. Although the residual carbon content in P4 rose to 59.3%, the synergy factor did not continue to decrease, and the crack area rebounded to 12.3%, indicating that after the outer layer’s rigidity increased too rapidly, the shell’s advantage began to be offset by interfacial traction.

Figure 9(b) further uses Ph/Si and Zr/Si as formulation coordinates, with post-heat strength at 500 ℃ serving as the bubble size. P0 and P1 are located in the low-aromaticity, low-zirconium region, with post-500 ℃ strengths of only 0.86 and 1.42 MPa, respectively; P2, with slight increases in Ph/Si and Zr/Si, exhibits a post-500 ℃ strength of 2.11 MPa; P3 is situated at Ph/Si = 0.40 and Zr/Si = 0.06, with a post-500 ℃ strength of 2.73 MPa, falling at the centre of the equilibrium window; When P4 further moves in the direction of higher aromaticity and higher zirconium content, therefore, its strength after 500 ℃ drops back to 2.41 MPa. These results indicate that the decomposition temperature alone is insufficient to determine the upper limit of the formulation; shell stiffness and interfacial mismatch also determine the boundaries of the window. Combining Figures 8 and 9, the acid-thermal synergistic ageing process can be summarised as four consecutive stages. The acidic medium first penetrates the gel layer along surface defects and edge micropores, causing hydrolysis of the Si-O-Si bonds and increasing the polarity of the surface layer; subsequently, during the thermal phase, dehydration condensation and the escape of oligomers occur in the damaged regions, gradually densifying

the surface layer; as the cycle continues, the residual shell containing Si/O/Zr begins to form sheet-like structures, the surface modulus increases, and a more pronounced gradient forms between the surface and the inner layer; in the later stages, shrinkage cracks and interfacial gaps expand simultaneously, and the fracture mode shifts from cohesive failure to mixed or interfacial failure.

4 Conclusion

This paper presents a systematic analysis of the formulation design, joint evaluation and acid-heat synergistic ageing mechanism of a 500 ℃ heat-resistant silicone adhesive, establishing a correlation between molecular structure and interfacial failure. The main conclusions are as follows.

(1) By adjusting the Ph/Si and Zr/Si ratios, a curable organosilicon network enriched in phenyl groups and containing Si-O-Zr nodes was constructed. The P3 formulation achieved a good balance between double bond conversion, delayed thermal weight loss, residual carbon content and high-temperature modulus retention; its T5% was 438 ℃, with a residual carbon content of 56.8% at 800 ℃, and a lap shear strength of 2.73 MPa following thermal exposure at 500 ℃, indicating that the key to 500 ℃-grade silicone adhesives lies in the simultaneous optimisation of residual layer continuity and load-bearing network retention.

(2) Strength degradation under acid-heat coupled conditions was significantly faster than under pure acid ageing or pure thermal ageing alone, but the extent of this degradation varied markedly between different formulations. P3 retained 59.2% of its initial strength after 15 cycles, with a synergy factor of 1.18. Mechanistic analysis indicates that the acidic medium first induces Si-O-Si hydrolysis and silanol enrichment at the surface and interfaces, whilst the subsequent thermal phase drives the damaged regions to undergo re-condensation and inorganic transformation; the continuity of the shell layer and the modulus gradient jointly determine whether cracks will further propagate and cause interfacial delamination.

(3) This paper proposes a failure map centred on the residual carbon content, synergy factor and retained strength after ageing, which can be used to distinguish between three states: insufficient residual layer, balanced shell and excessively hard shell. Current research remains focused primarily on single-lap joints in 304 stainless steel and mixed acid media; future work needs to incorporate longer thermal dwell times, external load coupling and multi-substrate interfaces to establish a life model that more closely approximates engineering conditions.

About the Author

Yaosheng Liang was born in Guangxi, PR China, in 1986. He graduated from Nanjing Tech University in 2009. Now, He works at Suzhou Nuclear Power Research Institute Co., Ltd. His main research area is polymer coatings.

Yongliang Sun was born in Henan, PR China, in 1986. He graduated from Xi’an Jiaotong University in 2010. Now, He works at Suzhou Nuclear Power Research Institute Co., Ltd. His main research area is polymer coatings.

Rong Sun was born in Sichuan, PR China, in 1995. He graduated from Sichuan University in 2023. Now, He works at Suzhou Nuclear Power Research Institute Co., Ltd. His main research area is polymer coatings.

References

[1] Xing, Y., Kang, H., Li, D., et al. (2024). An understanding of component-properties relationship of high-temperature resistant addition-cure liquid silicone rubber: A review. Polymer Degradation and Stability, 230, 111034.

[2] Robeyns, C., Picard, L., & Ganachaud, F. (2018). Synthesis, characterization and modification of silicone resins: An “augmented review”. Progress in Organic Coatings, 125, 287-315.

[3] Han, J., Mei, J., Huang, D., et al. (2024). SiO2 bridged AlN/methylphenyl silicone resin composite with integrated superior insulating property, high-temperature resistance, and high thermal conductivity. Journal of Colloid and Interface Science, 661, 91-101.

[4] Jiang, J., Yuan, X., Xue, K., et al. (2022). Novel hybrid zirconium-silicone resin as high-temperature adhesive and an insight into the thermal resistance mechanism. Chemical Engineering Journal, 446, 137350.

[5] Gu, Y., Li, T., Zhao, L., et al. (2024). Zirconium-modified organosiloxane resin for high-temperature-resistant coatings. Polymer, 307, 127302.

[6] Long, L., Cai, Y., Chi, X., et al. (2024). A novel molecular structure design of liquid silicone rubber modified by ceramic precursors for high-performance flexible ablation. Polymer Degradation and Stability, 225, 110775.

[7] Xue, J., Zhang, L., Hou, Y., et al. (2023). Polysilazane-based high-temperature adhesives for the joints of amorphous SiBON ceramic composites. Journal of Manufacturing Processes, 88, 220-231.

[8] Xue, J., Hou, Y., Zhang, L., et al. (2024). Synthesis of novel vinyl preceramic polymer (PBSZ) adhesives and their performances in ceramic joints. Ceramics International, 50(1), 1038-1049.

[9] Luan, X., Zhu, X., Dong, X., et al. (2024). Strengthened and toughened SiHfBCN-based high-temperature resistant adhesive with SiC NWs. Chinese Journal of Aeronautics, 37(7), 539-549.

[10] Xie, J., Sun, H. J., Zhang, X. Z., et al. (2015). Carborane-containing solvent-free liquid silicone resin: Synthesis, characterization, and high-temperature adhesive properties. Phosphorus, Sulfur, and Silicon and the Related Elements, 190(3), 277-291.

[11] Qin, Y., Rao, Z., Huang, Z., et al. (2014). Preparation and performance of ceramizable heat-resistant organic adhesive for joining Al2O3 ceramics. International Journal of Adhesion and Adhesives, 55, 132-138.

[12] Wang, X., Wang, J., & Wang, H. (2013). Performance and structural evolution of high-temperature organic adhesive for joining Al2O3 ceramics. International Journal of Adhesion and Adhesives, 45, 1-6.

[13] Feng, J., Zhang, Q., Tu, Z., et al. (2014). Degradation of silicone rubbers with different hardness in various aqueous solutions. Polymer Degradation and Stability, 109, 122-128.

[14] Zhang, Z., Zhang, Z., Yue, S., et al. (2023). Performance characteristics of silicone rubber for use in acidic environments. Polymers, 15(17), 3598.

[15] Gao, Y., Li, S., He, S., et al. (2024). Molecular dynamics supported thermal-moisture aging effects on properties of silicone rubber. Progress in Organic Coatings, 191, 108503.

[16] Ramram, M., Belec, L., Chailan, J. F., et al. (2025). Pressure steam ageing of silica filled silicone rubber: Degradation mechanisms. Polymer Degradation and Stability, 237, 111332.

[17] de Souza, F. B., Bautista, J., Giam, A., et al. (2025). Understanding degradation mechanism for long-term natural weathering of building silicone sealant to guide future façade design, inspection, and accelerated testing methods. Polymer Degradation and Stability, 236, 111299.

[18] Wu, J., Dong, J., Wang, Y., et al. (2017). Thermal oxidation ageing effects on silicone rubber sealing performance. Polymer Degradation and Stability, 135, 43-53.

[19] Li, G., Tan, J., & Gong, J. (2012). Chemical aging of the silicone rubber in a simulated and three accelerated proton exchange membrane fuel cell environments. Journal of Power Sources, 217, 175-183.

[20] Li, G., Tan, J., & Gong, J. (2012). Degradation of the elastomeric gasket material in a simulated and four accelerated proton exchange membrane fuel cell environments. Journal of Power Sources, 205, 244-251.

[21] Pehlivan-Davis, S., Clarke, J., & Armour, S. (2013). Comparison of accelerated aging of silicone rubber gasket material with aging in a fuel cell environment. Journal of Applied Polymer Science, 129(3), 1446-1454.

[22] Wu, F., Chen, B., Yan, Y., et al. (2018). Degradation of silicone rubbers as sealing materials for proton exchange membrane fuel cells under temperature cycling. Polymers, 10(5), 522.

[23] Lu, M., Zeng, S., Gao, C., et al. (2025). Aging analysis of HTV silicone rubber under coupled corona discharge, humidity and cyclic thermal conditions. Electronics, 14(20), 4071.

[24] Tang, Y. H., Liu, J., Chen, Z. Y., et al. (2024). Recent advances in fire-retardant silicone rubber composites. Polymers, 16(17), 2442.

[25] Ding, W., Yan, L., Huang, M., et al. (2023). In-situ constructing SiC frame in silicone rubber to fabricate novel flexible thermal protective polymeric materials with excellent ablation resistance. Polymer, 285, 126319.